



OPEN Treatment of non-small cell lung cancer using chem-bioinformatics-driven engineering of exosomal cargo-vehicle for telmisartan and pioglitazone targeted-delivery

Nadia M. Hamdy¹✉, Eman F. Sanad¹, Shaymaa E. Kassab^{2,3}✉, Merhan Essam¹, Monica A. Guirguis⁴, Emad B. Basalious⁶ & Ahmed S. Sultan^{4,5}

The activation of the PPARG transcription factor is linked to reduced non-small cell lung cancer (NSCLC) growth. Bioinformatics, cheminformatics, and molecular docking/dynamics studies assessing pioglitazone and telmisartan as repurposed PPARG agonists for treating NSCLC with a targeted delivery system was done. Bioinformatics confirmed that the expression of the PPARG gene can predict outcomes in lung adenocarcinoma and is related to immune cells present in the tumor. Cheminformatics data showed that pioglitazone and telmisartan have a strong attraction to the PPARG receptor, with good efficiency as ligands. Both drugs were found to be lipophilic, suggesting compatibility with a targeted delivery formulation that may include albumin. Further cheminformatics predictions highlighted systemic toxicity values and the need for targeted delivery to minimize toxic side effects. Molecular docking and dynamics simulations showed that the telmisartan-MyoVc cargo domain complex was strong and stable during an 18 ns simulation period. Bioinformatics and cheminformatics data support pioglitazone and telmisartan as promising repurposed drugs for LUAC, highlighting their lipophilicity and compatibility with exosomal components like albumin. Cheminformatics also pointed out potential off-target effects and hepatotoxicity, emphasizing the importance of exosomal targeted delivery. Molecular docking and MD simulations confirmed the affinity and stability of drug-exosomal vehicle complexes. The proposed engineering of exosomal cargo for targeted delivery of these drugs to lung cells could enhance NSCLC treatment and address drug resistance while minimizing systemic toxicity.

Keywords Bioinformatics, Cheminformatics, Pioglitazone, Telmisartan, Lung adenocarcinoma, Exosomes, PPARG, Targeted delivery, Molecular Docking, In Silico drug repurposing

Abbreviations

ABCB11	Bile salt export pump
ACE	Angiotensin-converting enzyme
ADMET	Absorption, distribution, metabolism, excretion, and toxicity
AGTR1	Angiotensin II receptor 1
AGTR1B	Angiotensin II receptor 1B
AGTR2	Angiotensin II receptor 2
AMs	Adhesion molecules
Ang2	AngII: Angiotensin II

¹Department of Biochemistry, Faculty of Pharmacy, Ain Shams University, Abassia 11566, Cairo, Egypt.

²Department of Pharmaceutical Chemistry, Faculty of Pharmacy, Damanshour University, Damanshour 22516, Egypt.

³Protac Scientific, Drug Discovery Pro LLC, Cairo 11627, Egypt. ⁴Biochemistry Department, Faculty of Science, Alexandria University, El- Shatbi 21568, Alexandria, Egypt. ⁵Department of Oncology, Lombardi Comprehensive Cancer Center, Georgetown University Medical Center, Washington, DC, USA. ⁶Department of Pharmaceutics and Industrial Pharmacy, Faculty of Pharmacy, Cairo University, Al Kasr AlAiny, Cairo 11562, Egypt. ✉email: nadia_hamdy@pharma.asu.edu.eg; shaymaa.kassab@pharm.dmu.edu.eg

ARB	Angiotensin II Receptor Antagonist
AT1	Angiotensin II type 1 receptors
BBB	Blood brain barrier
BP	Blood Pressure
CA2	Carbonic anhydrase 2
CF	Cystic Fibrosis
COPD	Chronic Obstructive Pulmonary Diseases
DB	Database
DC	Dendritic Cells
DDPD	Digital drug property database
DDS	Drug Delivery Systems
ECM	Extracellular matrix
ECVs	Extracellular vesicles
EPT	Effective-Personalized-Targeted
GBSA	Generalized Born and Surface Area solvation
GFs	Growth factors
GLRA1	Glycine receptor subunit alpha-1
H-bonds	Hydrogen bonds
HAS	Human serum albumin
HSP90	Heat Shock Protein 90
HTN	Hypertension
ImmuCellAI	Immune Cell Abundance Identifier
iTDDS	Innovative Drug delivery system
KEGG	Kyoto Encyclopedia of Genes and Genomes
L.E	Ligand efficiency
LogP	Partition coefficient
LUAD	Lung Adenocarcinoma
MAOB	Monoamine oxidase B
MD	Molecular dynamics
MM	Molecular Mechanics
MOE	Molecular Operating Environment
Mwt	Molecular weight
MyoV, VC,5C	Myosin V, VC, 5 C
NAMD	Nanoscale Molecular Dynamics
NCBI	National Center for Biotechnology Information
NCDs	Non-communicable diseases
NK	Natural killer cells
NR	Nuclear receptors (NR) ligands
NSCLC	Non-Small Cell Lung Cancer
NT	Nanotechnology
o/w	Octanol-water
PAH	Pulmonary Arterial Hypertension
PDB	Protein Data Bank
PEG	Polyethylene glycol
PLGA	Poly(lactic-co-glycolic acid)
PPAR-gamma/PPARG	Peroxisome Proliferator-Activated Receptor Gamma
PPARA	Peroxisome Proliferator-Activated Receptor Alpha
PPI	Protein-Protein Interaction
QM	Quantum Mechanics
QSAR	Quantitative Structure-Property Relationships
RMSD	Root-Mean Square Deviations
SCLC	Small Cell Lung Cancer
SEA	Similarity Ensemble Approach
SIB	Swiss Institute of Bioinformatics
SMILES	Simplified Molecular Input line entry specification
TCGA	The Cancer Genome Atlas
TDD	Targeted Drug Delivery
TDDS	Targeted Drug delivery system
TISIDB	The integrated repository portal for tumor-immune system interactions
TPSA	Topological polar surface area
TZDs	Thiazolidinediones

Problem statement

The creation of an effective system/formula for treating lung cancer is critical, especially given the annual increase in new cancer cases.

Literature review

Cancer-related fatality impedes progress toward Sustainable Development Goal (SDG) #3 of “Better Health.”

As the field of drug delivery systems (DDS) has evolved, nanotechnology (NT) has made significant contributions to the development of smart nanocarriers^{1,2} such as synthetic lipid-based nanocarriers that provide a unique platform for drug encapsulation^{3,4}. Furthermore, natural cell-derived carrier systems have sparked substantial interest⁵.

The lncRNADisease database⁶ and the Kyoto Encyclopedia of Genes and Genomes (KEGG) database⁷ include these types of lung cancer: lung adenocarcinoma (LUAD), lung cancer that has spread to the brain, lung squamous cell carcinoma, pulmonary adenocarcinoma, non-small cell lung cancer (NSCLC), and small cell lung cancer (SCLC). Genetic changes in the lung and related pathways (Fig. 1) from KEGG include Ras or ErbB, MAPK (mitogen-activated protein kinase), calcium, and PI3K-AKT signaling pathways, which are linked to oncogenes or tumor suppressor genes.

Interestingly, both in vitro^{8–10} and in vivo¹¹ studies have shown that activating peroxisome proliferator-activated receptor gamma (PPARG) slows down the growth of NSCLC lung cancer cells and/or might help stop the spread of developed NSCLC¹². KEGG data on lung cancer genetic pathways that matched the results of earlier experimental studies, which demonstrated MAPK's regulatory capability over PPARG activity^{13, 14, 15} providing proof-of-concept for the direction of our research.

Repositioning diverse pharmaceuticals with distinct modes of action is a strategic approach to mitigate or postpone cancer treatment resistance¹⁵. Selective PPARG activators have been previously investigated for their roles as antidiabetic agents or insulin sensitizers and their involvement in lipid metabolism^{16, 17}. The efficacy of thiazolidinediones (TZDs), a category of oral PPARG activators that mitigate tumor growth progression in the liver¹⁸ and in NSCLC xenograft animal models^{11, 19, 20}, has been established for decades. BioGRID^{4, 421} and the integrated repository portal for tumor-immune system interactions (TISIDB)²² consistently identified pioglitazone as a distinctive interactor of PPARG, classified as a member of TZDs with the most extensive safety margin. Telmisartan, an angiotensin II receptor type 1 (AT1) antagonist, utilized in hypertension management, was identified as a partial PPARG agonist^{23–25}. Moreover, recent studies have demonstrated the anticancer properties of telmisartan against many cancer types, including NSCLC^{26–28}. Unexpectedly, the PI3K/AKT signaling pathway²⁸ contributed to the anticancer efficacy of telmisartan against NSCLC with PPARG activation, aligning with the lung oncogenes depicted in Fig. 1.

The use of exosomes, as a regenerative-biological cell therapy, shows promise for treatment of various non-communicable diseases (NCDs)²⁹. We will use exosomes to transport natural or manufactured anticancer drugs, to tumor cells as safe and non-immunogenic way^{30–32}. It would be more appropriate to utilize exosomes, which are naturally occurring extracellular vesicles (ECVs) in the blood or tissues, instead of drug-encapsulated nano-scaffolds made of blended FDA-approved polymers like polyethylene glycol (PEG) or polylactic-co-glycolic acid (PLGA).

Online databases Vesiclepedia and Exocarta³³ show that exosomes, which are a type of extracellular vesicle (ECV), contain parts of cell membranes, such as transmembrane proteins, surface markers, albumin, growth factors and their receptors, proteoglycan receptors, cytokines, heterotrimeric G proteins, heat shock protein 90

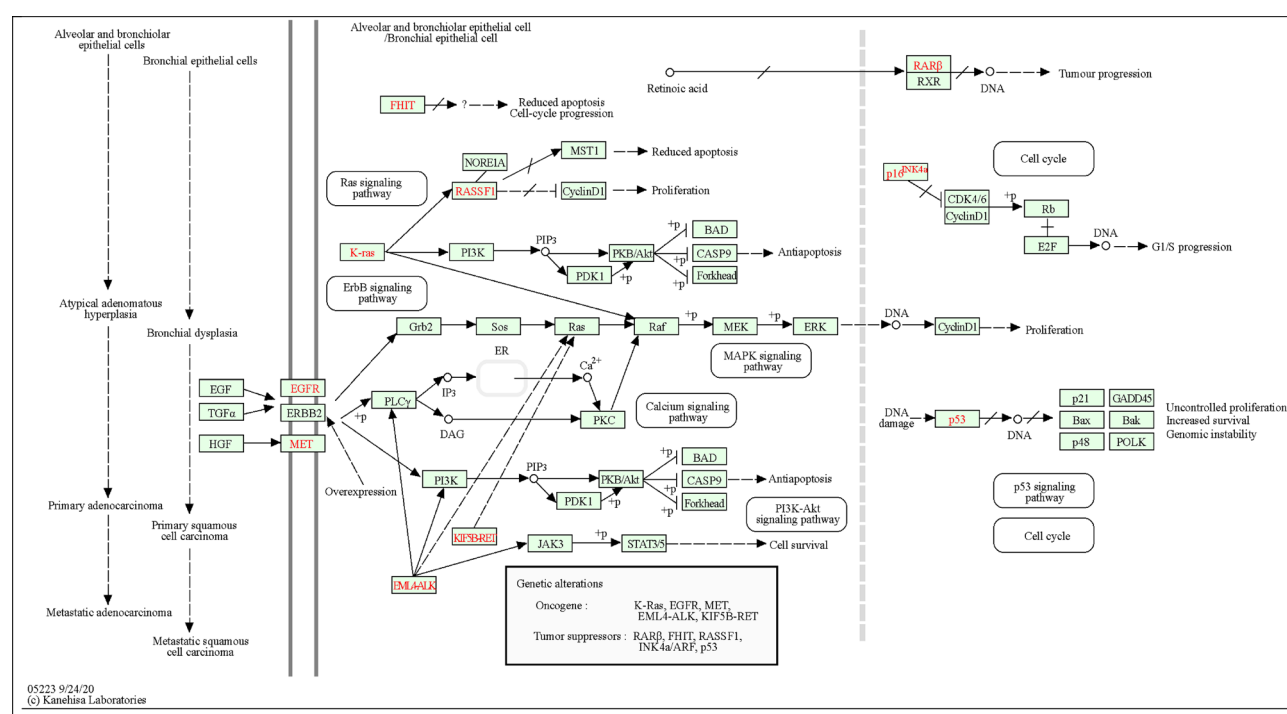


Fig. 1. Lung genetic alterations and related pathways retrieved from KEGG, where Ras or ErbB, MAPK, calcium, and PI3K-AKT signaling pathways comprising either oncogenic or tumor suppressor genetic alteration signaling pathways give rise to atypical hyperplasia, then primary and metastatic adenocarcinoma.

(HSP90), and non-muscle myosin³⁴. This non-muscle myosin probably works with cytoskeletal actin in target organs, along with adhesion molecules and proteins from the extracellular matrix.

Aim and objectives

Per, we emphasize pioglitazone and telmisartan as distinctive ligands for the NSCLC repressor PPARG in the current in-silico targeted delivery investigation; therefore, we will use chem-bio-informatics³⁵ to find out how well the chosen drugs work for treating lung cancer when delivered by exosome cargo, before testing them in the lab.

Second, to establish the drug's affinity for the carrier protein, we will run the test drugs through a stiff molecular docking process in the exosome cargo domain, using albumin as a protein component of the target exosome. In addition, we will run a molecular dynamics simulation on the drug-cargo combination to see how stable it is when interacting with the protein in the drug delivery system.

Materials and methods

Bioinformatics databases

Biological information

Transcriptome data and clinical information for LUAD were gathered from The Cancer Genome Atlas (TCGA) using the Genomic Data Commons download tool.

Lung cell type enriched transcriptome

The Human Protein Atlas³⁶ shows that the lung-specific proteome has 195 raised genes, 17 enriched genes, and 42 group-enriched genes. The Human Protein Atlas gave us the results acquired from the following links:

<https://genemania.org/search/homo-sapiens/pparg>.
<http://stitch.embl.de/cgi/network.pl?%20taskId=KpczawHjZrz>.
<https://thebiogrid.org/111464/summary/homo-sapiens/pparg.html>.

Systematic data base-mining and enrichment-analyses of PPARG gene expression profile and prognostic role in lung adenocarcinoma (LUAD)

UALCAN data base mining The open-access platform UALCAN (<http://ualcan.path.uab.edu/>) is based on level 3 RNA-seq and pathological files from the TCGA database³⁷ and was used to examine the relative transcriptional levels of the PPARG gene between tumor and non-cancerous tissues, as well as the correlation of PPARG gene mRNA levels with pathological features.

Differential expression of PPARG gene in LUAD and normal tissues We are looking at how much PPARG is expressed in normal tissues compared to tumor tissues using data from the GTEx Portal^{38,39} Release V8, which can be found at this link: https://expheas.ca/v1/gene/ENSG00000132170?analysis_subset=BOTH#cardio-end-points-results-section.

<https://www.gtexportal.org/home/gene/ENSG00000132170>.

<http://ualcan.path.uab.edu/cgi-bin/TCGAExResultNew2.pl? genenam = PPARG&ctype = LUAD>.

The expression of the PPARG gene in LUAD is shown according to the type of tumor, its stage, whether it has spread to lymph nodes, and the mutation status of the TP53 protein. <https://ualcan.path.uab.edu/cgi-bin/TCGAExResultNew2.pl? genenam = PPARG&ctype = LUAD>.

The TP53 mutation status was determined using whole exome sequencing data from TCGA, which was obtained via Mutation Annotation Format (MAF) files generated by VarScan2 on the Genomic Data Commons portal. The samples with and without the TP53 mutation were matched to RNA-seq data.

GEPiA database mining GEPiA, an interactive website (<http://gepia.cancer-pku.cn/>) Using data from the Cancer Genome Atlas and the TCGA database, “expression level analyses”⁴⁰ were conducted to study the prognostic values and survival related to PPARG gene expression in lung cancer and nearby normal tissue samples. The gene expression patterns of the PPARG-correlated genes are also extracted and rated alongside PPARG. We acquired the data results from the following link: <https://ualcan.path.uab.edu/cgi-bin/TCGAExHeatMap5KK.pl?%20cantype=LUAD&correlFile=PPARG%23%23QlWdS8a2H>.

ImmuCellAI analysis The Immune Cell Abundance Identifier (ImmuCellAI) program, <http://bioinfo.life.hust.edu.cn/ImmuCellAI>, calculates the abundance of 24 immune cells from gene expression datasets obtained by RNA-Seq and microarray data⁴¹.

The 24 immune cells are divided into 18 T-cell subtypes and six other types: B cells, natural killer (NK) cells, monocyte cells, macrophage cells, neutrophil cells, and dendritic cells. The 24 immune cells are divided into two layers: innate immunity, which includes DC, B cells, monocytes, macrophages, NK, neutrophils, CD4 T, CD8 T, NKT, and Tgd. Layer 2 of adaptive immunity includes CD4 naive, CD8 naive, Tc, Tex, Tr1, nTreg, iTreg, Th1, Th2, Th17, Tfh, Tcm, Tem, and MAIT.

We obtained the expression data for the 24 immune infiltrating cells corresponding to LUAD samples from the ImmuCellAI website. The revised database includes an R package for retrieving heatmap and pairwise correlation matrix visualizations. The database application is called Tumor Immune Estimation Resource (TIMER 2.0).

<https://cistrome.shinyapps.io/timer/> is a web server that brings together resources for studying immune cell abundance and gene expression in LUAD⁴². We validated the ImmuCellAI data using the TIMER 2.0 database and found it to be supportive.

The GEPIA database, <http://gepia.cancer-pku.cn/>, provides correlation curves between PPARG expression levels and immune infiltration of tumor-infiltrating lymphocytes, CD8 + T cells, CD4 + T cells, macrophages, neutrophils, and dendritic cells in LUAC.

PPARG protein-protein interaction and functional network

The Protein-Protein Interaction (PPI) network was constructed using GeneMANIA version 3.6.0 <http://www.genemania.org/>⁴³ Utilizing a massive collection of functional association data to predict PPARG gene function and discover additional genes connected to PPARG, BioGRID⁴⁴ database <https://thebiogrid.org/> and STITCH version: 5.0 <http://stitch.embl.de/> Protein and genetic relationships, pathways, co-expression, co-localization, and protein-domain similarity are all association data used to draw the rank showing important interacting molecules. The data obtained from GeneMANIA and STITCH for the PPARG network of predicted functional partners met the results obtained from BioGRID⁴⁴ <https://thebiogrid.org/111464/summary/homo-sapiens/ppa.html> (Accessed April 20th, 2024).

The data could be visualized through these links:

GeneMANIA network: <https://genemania.org/search/homo-sapiens/pparg>.

STITCH network: <http://stitch.embl.de/cgi/network.pl?%20taskId=KpczawHjZrz>.

BioGRID⁴⁴ network: <https://thebiogrid.org/111464/summary/homo-sapiens/pparg.html> (Accessed April 20th, 2024).

Molecular docking

Polar hydrogens were added to the resulting PDB files⁴⁴, and docking was carried out using the Molecular Operating Environment (MOE) version 2014.0901 software (Chemical Computing Group Inc., Quebec, Montreal, Canada).

https://www.chemcomp.com/Research-Citing_MOE.htm.

We treated the protein to remove repeated chains and water molecules. The MOE QuickPrep methodology was used to refine the structure, 3D protonation, and partial charge calculation using an RMSD gradient of 0.1 kcal/mol and the AMBER10:EHT field.

In this study, we employed rigid docking to calculate the binding affinity scores (KJ/mol) of pioglitazone and telmisartan to albumin and extracellular exosomes, which serve as carrier proteins for targeted lung medicine administration.

For the MyoVc carrier protein, we used the SiteFinder | 3D server's site finder tool⁴⁵ to find the largest pocket with 57 amino acids, verifying that the tested drugs fit well.

We used the MOE Dock protocol and its descriptors to establish the optimum postures and binding score values for the drugs under investigation. We ran molecular docking with the MOE default settings, using the triangle matcher as the placement method and London dG as the primary scoring function. We added another refinement step by integrating the stiff docking approach with the GBVI/WSA dG affinity score algorithm⁴⁶. Furthermore, the test compound's first docking pose was the best, with the highest binding energy value. The best pose was finally chosen, photographed, and exported as a JPEG.

MD simulation of telmisartan in cargo binding domain from human MyoVc

A molecular dynamics simulation of telmisartan was performed for 18 ns, demonstrating the drug's stability within the cargo-binding region of the human carrier protein MyoVc (PDB code: 4L8T), which is crucial for the exosome's cargo. Molecular dynamic simulations employed Molecular Mechanics with Generalized Born and Surface Area solvation method (MM/GBSA) to calculate the free energy of ligand binding to proteins (Godschalk et al., 2013).

The initial PDB files for the optimal pose of the telmisartan compound in complex with the protein were prepared for the run. MD simulations were conducted for 19 nanoseconds at 310 K, equivalent to body temperature, utilizing Nanoscale Molecular Dynamics (NAMD 2.14 Release - Aug 2020) software <https://www.ks.uiuc.edu/Research/namd/>, which is founded on the Charm++ programming model. The pH was kept at a standard physiological level of 7. We employed the all-hydrogen AMBER99SB force field to accurately represent molecular interactions. The geometry of telmisartan was optimized through quantum mechanics (QM) calculations using Gaussian 16 software <https://gaussian.com/gaussian16/>, and the Schrödinger equation was solved for the molecule⁴⁷. The input consists of the coordinates, net charge, and total spin. The outcome comprises the total energy and the wave function, which serve as the basis for calculating all measurable properties of the system.

The final charges for Telmisartan were assigned to the compound utilizing Antechamber, and the force field parameters adhered to GAFF2 standards⁴⁸. The general AMBER force field is utilized for rational drug design, as detailed on the official website, ensuring precise modeling of molecular forces. The complex was located centrally within a traditional three-point water model, the TIP3P water cube, with dimensions that provided a minimum 14 Å water buffer surrounding the complex. To replicate physiological conditions, the complex was neutralized and adjusted to a 150 mM ionic concentration of sodium and chloride ions, accomplished by replacing water molecules with the highest electrostatic potential at their oxygen atoms with these ions. The current MD protocol commenced with an initial depreciation of the fully solvated and ionized systems, succeeded by a gradual temperature increase to the target level. We imposed substantial constraints on the protein backbones and bound telmisartan to avoid unrealistic modifications during the initial simulation phases. Following heating, the systems experienced a 1 ns equilibration under periodic boundary conditions, during which energy restraints were gradually lifted. The simulations continued for an additional 17 ns, recording atomic coordinates at intervals of 0.1 picosecond for comprehensive analysis. This experimental method for

molecular dynamics provided a controlled simulation environment, essential for accurately investigating the dynamics and stability of the human myosin cargo binding domain and telmisartan complex.

Results and discussion
Bioinformatics studies

This study is part of a bigger project in our group that uses natural products that have been changed into new uses, like prodigiosin, camptothecin, and hinokitiol, to target different types of cancer^{49–51}. The project also uses man-made small-molecule drugs that target signaling pathways in diseases like cancer^{52,53}.

Two drugs called pioglitazone and telmisartan⁵⁴ are known to trigger PPARG. This study investigated whether they could help cure lung cancer by using exosomes. Exosomes that cells release could be used to deliver drugs for the focused treatment of certain diseases^{55,56}.

Before doing any experiments in cells or living things, we used computer analysis, bioinformatics, cheminformatics, molecular modeling, and simulation to guess how the two PPARG agonist drugs would react and interact with their target molecules in lung cancer, as well as with proteins and drug cargo. This assumption was very important before making the drug-exosomal cargo for the lungs. It made sure that it was only taken up by lung cancer cells so that the drug could be given in a controlled and long-term way to create an “effective, personalized, and targeted” (EPT) treatment.

Lung cell type enriched transcriptome

The Human Protein Atlas indicates that the lung has the most group-enriched gene expression similarity to lymphoid tissue, with the PPARG gene being one of the enriched genes expressed in the lung. Table 1 presents the number of genes within each specificity group for the lung cell types.

Systematic database mining and enrichment-analyses of PPARG gene expression profile and the prognostic role in lung adenocarcinoma (LUAD)

Utilizing the UALCAN database³⁷ associated with the GTEx database gateway, we examined the expression levels of the PPARG gene in normal and lung cancer cells, revealing that it is expressed at elevated levels in normal tissues relative to malignant tissues (Fig. 2).

Figure 2 illustrates PPARG gene expression based on sample type, using TCGA samples to compare primary lung tumors ($n=515$) with 59 normal samples, as analyzed by UALCAN, and indicates statistical significance (A). The median gene-level TPM is 19.5 for the lung (green line pointing to 8 o'clock) for 578 samples. (B) The violin plot and (C) the box plot illustrates that the PPARG gene is expressed at higher levels in lung-normal tissue from 59 cases compared to tumor tissue from 515 cases.

PPARG gene expression plots (Fig. 3) based on tumor histology (Fig. 3A), tumor stage (Fig. 3B), nodal metastasis (Fig. 3C), and tissue TP53 mutation status (Fig. 3D) verified the significantly higher levels of gene expression in normal lung cells and tissues compared to the different histological features of LUAC and the lung tumor tissues at stages 1–4, respectively. PPARG gene expression was consistently higher in normal cases than in LUAC cases, regardless of whether they had absent or positive lymph nodal metastases and whether their TP53 status was non-mutated or mutated. The data presented in this phase of bioinformatics also demonstrates the role of PPARG gene activation in lung tissue protection against LUAC proliferation and metastases.

Figure 3. is using TCGA samples, we assessed the transcript/million of the PPARG gene in LUAD according to histological subtypes (A), individual cancer stages (B), nodal metastasis (C), and TP53 mutation status (D). [NOS: Lung Adenocarcinoma—Not Otherwise Specified; Mixed: Lung adenocarcinoma Mixed subtype with transparent cells: lung The condition is known as clear cell adenocarcinoma. LBC Nonmucinous: Lung Bronchioloalveolar

Lung cell type	Number of enriched genes			Total number enriched
	Very high	High	Moderate	
Respiratory ciliated cells	591	53	37	681
Alveolar cells type 1	43	41	48	132
Alveolar cells type 2	20	122	221	363
Mitotic cells	111	26	16	153
NK-cells	3	13	39	55
B-cells	4	1	6	11
Endothelial cells	0	9	88	97
Smooth muscle cells	14	13	36	63
Fibroblasts	28	64	164	256
Macrophages	4	51	105	160
Neutrophils	61	52	47	160
Mast cells	10	4	3	17
T-cells	6	29	54	89
Plasma cells	166	15	4	185
All cell types	1061	493	868	2422

Table 1. Number of genes in each specificity category in the lung cell types.

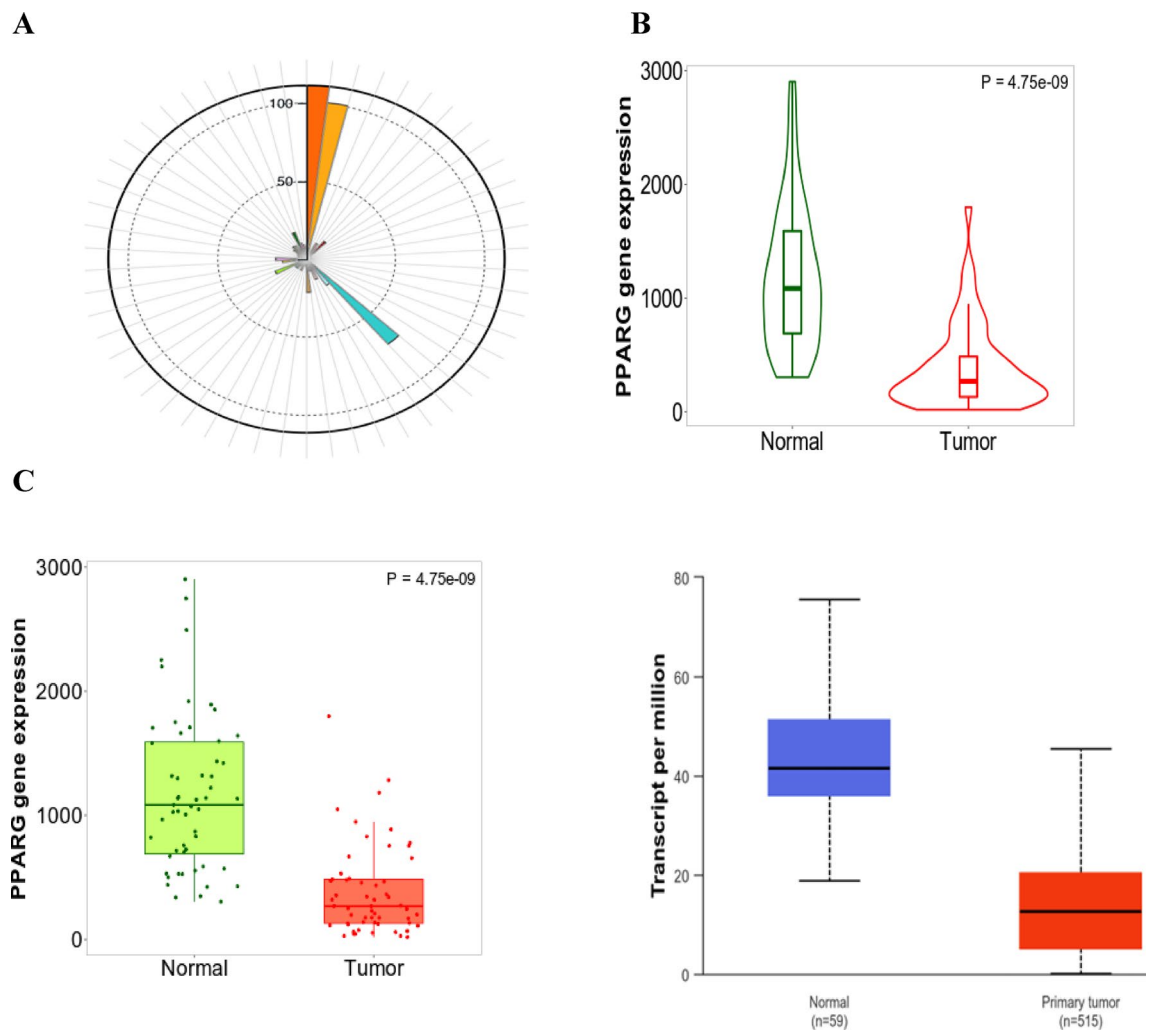


Fig. 2. PPARG gene expression based on sample type, from TCGA samples, comparing primary lung tumor ($n = 515$) to 59 normal samples, by UALCAN, showing statistical significance (A) median gene-level TPM is 19.5 for the lung (green line pointing to 8 o'clock) for 578 samples. (B) violin plot and (C) box plot showing the higher expression of the PPARG gene in lung-normal tissue for 59 cases compared to tumor tissue for 515 cases.

Carcinoma. A solid pattern in the lung is a defining feature of non-mucinous adenocarcinoma. Acinar: Lung. Acinar adenocarcinoma, LBC-mucinous: lung bronchoalveolar carcinoma. Mucinous (colloid) Carcinoma Papillary: Lung papillary adenocarcinoma. Mucinous: Lung Mucinous adenocarcinoma. Micropapillary: Lung micropapillary adenocarcinoma. Signet Ring: Lung. Signet Ring Adenocarcinoma. N0: No regional lymph node metastasis; N1: Metastases in 1 to 3 axillary lymph nodes; N2: Metastases in 4 to 9 axillary lymph nodes; N3: Metastases in 10 or more axillary lymph nodes; nodal metastasis is not available for one sample. NX: Eleven samples failed to detect cancer in the neighbouring LN.

The heatmap of PPARG gene expression in LUAC and other related genes revealed that PPARG is the most important gene associated with LUAC's poor prognosis, particularly when compared to normal tissue (Fig. 4) from the GEPIA database.

Additionally, ImmuneCellAI⁴¹ is used to gather expression data from 24 types of immune infiltrating (TIF) cells in LUAD samples to find and categorize the TIF cell subtype that has strong links to LUAC.

The new database includes an R tool for retrieving the pairwise correlation matrix (Fig. 5A) and heatmap (Fig. 5B) visualizations. Furthermore, examining the immune infiltration cell abundance in 576 ImmuneCellAI samples (Fig. 5B) revealed high levels of expression of macrophages, NK, DC, and other T-cell subtypes, which is corroborated by results from the TIMER 2.0 database program⁴². Additionally, the pairwise correlation matrix showed a strong connection between T-cell subtypes, macrophages, and DCs (Fig. 5A).

Accordingly, we studied the correlation of the PPARG gene expression level to the tumor-infiltrating lymphocytes, CD8+, CD4+, macrophages, neutrophils, and dendritic cells in LUAC as an excellent sign for cancer disease prognosis⁵⁷. Surprisingly, the gene expression was negatively correlated to B cells and positively correlated to CD8+ and CD4+ subtypes of T-lymphocytes in terms of the partial correlation values (Spearman's rho) obtained from the GEPIA database (Fig. 6).

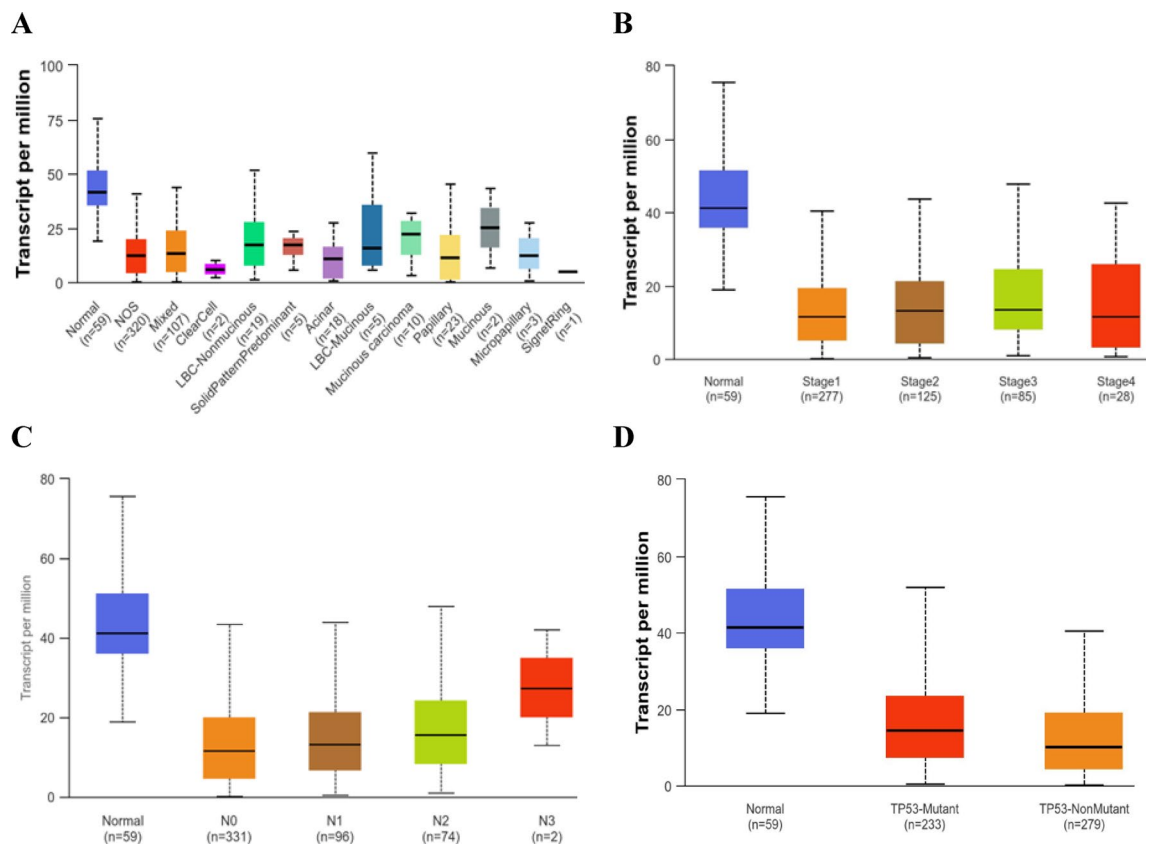


Fig. 3. PPARG gene Expression in transcript/million in LUAD based on histological subtypes (A), individual cancer stages (B), nodal metastasis (C), and TP53 mutation status (D), from TCGA samples. [NOS: Lung Adenocarcinoma-Not Otherwise Specified, Mixed: Lung Adenocarcinoma Mixed subtype, Clear Cell: Lung Clear Cell Adenocarcinoma, LBC-Non mucinous: Lung Bronchioloalveolar Carcinoma Non-mucinous, Solid Pattern Predominant: Lung Solid Pattern Predominant Adenocarcinoma, Acinar: Lung Acinar Adenocarcinoma, LBC-Mucinous: Lung Bronchioloalveolar Carcinoma Mucinous, Mucinous: Mucinous (Colloid) Carcinoma, Papillary: Lung Papillary Adenocarcinoma, Signet Ring: Lung Signet Ring Adenocarcinoma, N0: No regional lymph node metastasis, N1: Metastases in 1 to 3 axillary lymph nodes, N2: Metastases in 4 to 9 axillary lymph nodes, N3: Metastases in 10 or more axillary lymph nodes, nodal metastasis is not available for 1 sample, NX: cancer in nearby LN cannot be measured in 11 samples.].

To better understand how the PPARG gene functions in LUAD, we examined critical genes that interact with it via gene-protein linkages and gene-gene links, as well as creating and analyzing a PPI network.

Therefore, drugs such as pioglitazone and telmisartan can stimulate the PPARG protein, potentially aiding in the destruction of cancer cells⁵⁸ either by affecting genes or through pathways related to PPARG that were identified via computer analysis (Fig. 7).

Cheminformatics studies of the repurposed Pioglitazone and Telmisartan

*In-silico measurement of physicochemical properties and Tox21*⁵⁹

We used the Admetlab 2.0 online tool to assess the physicochemical features of pioglitazone and telmisartan, such as logP (lipophilicity) and TPSA (topological polar surface area). We also investigated how well the drugs bind to plasma proteins, their ability to cause breathing problems, their effects on mitochondrial membrane potential, aromatase enzyme activity, aryl hydrocarbon receptor activity, human liver toxicity, and liver injury caused by drugs used to treat the same drugs.

According to the results in Table 2, pioglitazone (logP=3.01) and telmisartan (logP=6.249) are both effective in mixing with fats, but telmisartan performs better. The TPSA values for pioglitazone (68.290 Å²) and telmisartan (72.940 Å²) indicate that these drugs can mix with lipids, but not adequately enough to pass through the blood-brain barrier, keeping them safe from possible side effects in the central nervous system. The TPSA values of pioglitazone (68.290 Å²) and telmisartan (72.940 Å²) revealed that these test drugs are lipophilic but not adequate to penetrate the blood-brain barrier (BBB), making them safe regarding any potential central nervous system (CNS) side effects^{62,63}. These findings also demonstrated that telmisartan and pioglitazone may be employed efficiently in targeted delivery systems based on various fat-loving materials, such as albumin and lung exosomes (Lung-Exo), without producing any physical problems.

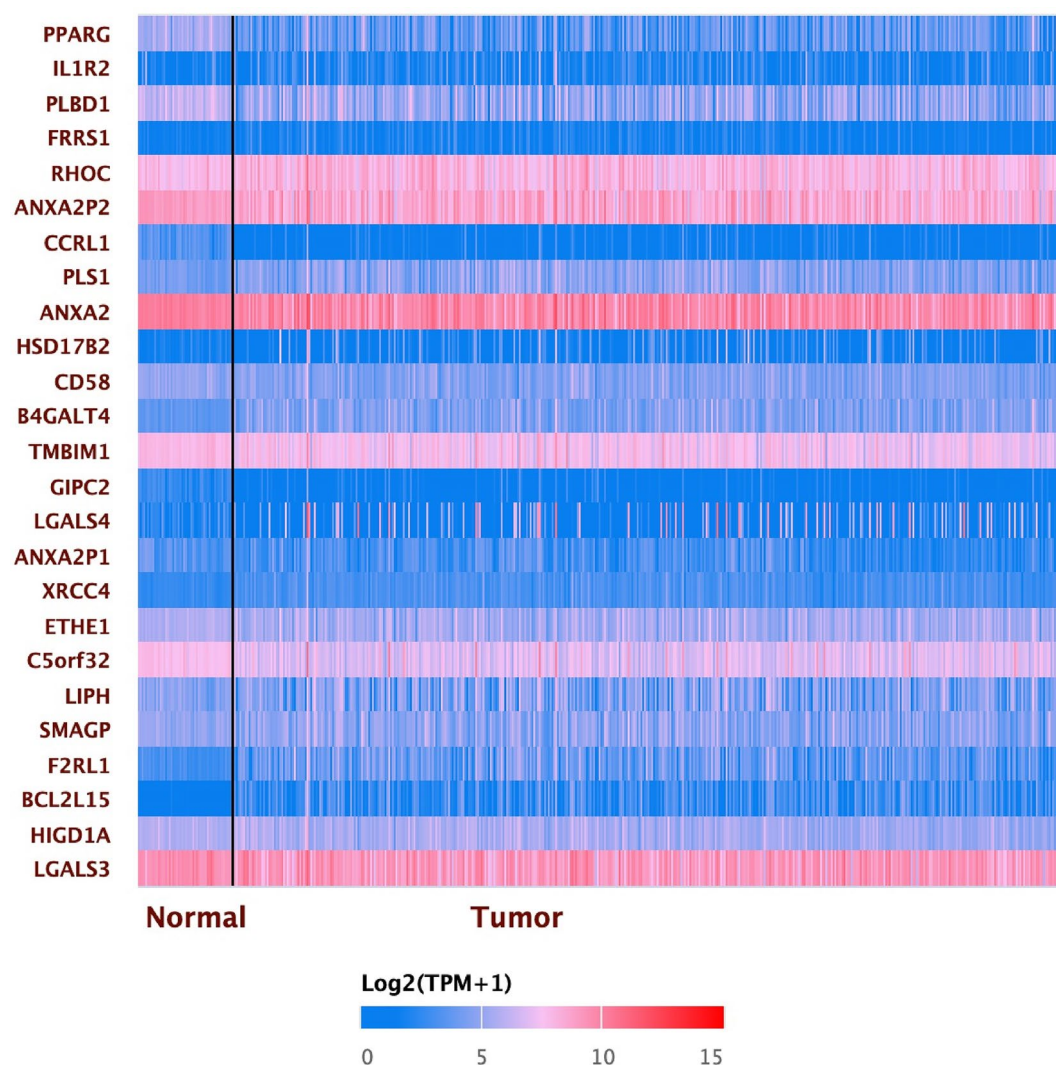


Fig. 4. Heatmap of the expression pattern of PPARG and other input genes in LUAD is positively correlated to the PPARG gene.

Based on computer estimates of how dangerous compounds are from the Tox21 Data Challenge, which is part of the NIH and FDA's "Toxicology in the 21st Century" initiative, we determined that pioglitazone, like telmisartan, affects SR-MMP activity (Table 2). Notably, investigations have demonstrated that pioglitazone causes mitochondrial damage, supporting the predictions (Table 2). Interestingly, experimental evidence⁶⁴ reveals that pioglitazone's mitochondrial toxicity fits expectations (Table 2). The test compounds demonstrated activity on NR-Aromatase and NR-AhR, both of which are part of the TOX21 pathway. The projected results (Table 2) indicated that pioglitazone and telmisartan had the potential to cause hepatotoxicity and drug-induced liver damage. Some experimental research^{65,66} demonstrated pioglitazone's ability to generate hepatic energy alterations, which validated the data given in Table 2.

Pioglitazone and Telmisartan biological targets of the highest corresponding probabilities

Using the Swiss Target Predictor^{67,68}, we discovered that pioglitazone and telmisartan are likely to interact with various biological targets, including receptors, enzymes, and transporter proteins (Table 3). Both drugs were shown to influence the liver bile salt export pump, the kidney enzyme carbonic anhydrase II (CA2), and the lung angiotensin-converting enzyme (ACE). The interactions match the known harmful effects of pioglitazone^{65,66} and telmisartan⁶⁹ along with the expected information from Admetlab 2.0^{60,61} about liver toxicity and damage (Table 2). The predictor determined that both drugs target the type-1 angiotensin II receptor (AGTR1) (Table 3). The findings imply that pioglitazone should be investigated for its potential as an AGTR1 binder, which could shed light on the structural properties that allow both telmisartan and pioglitazone to have the pharmacological effects of PPARG agonists and possibly AGTR1 antagonists.

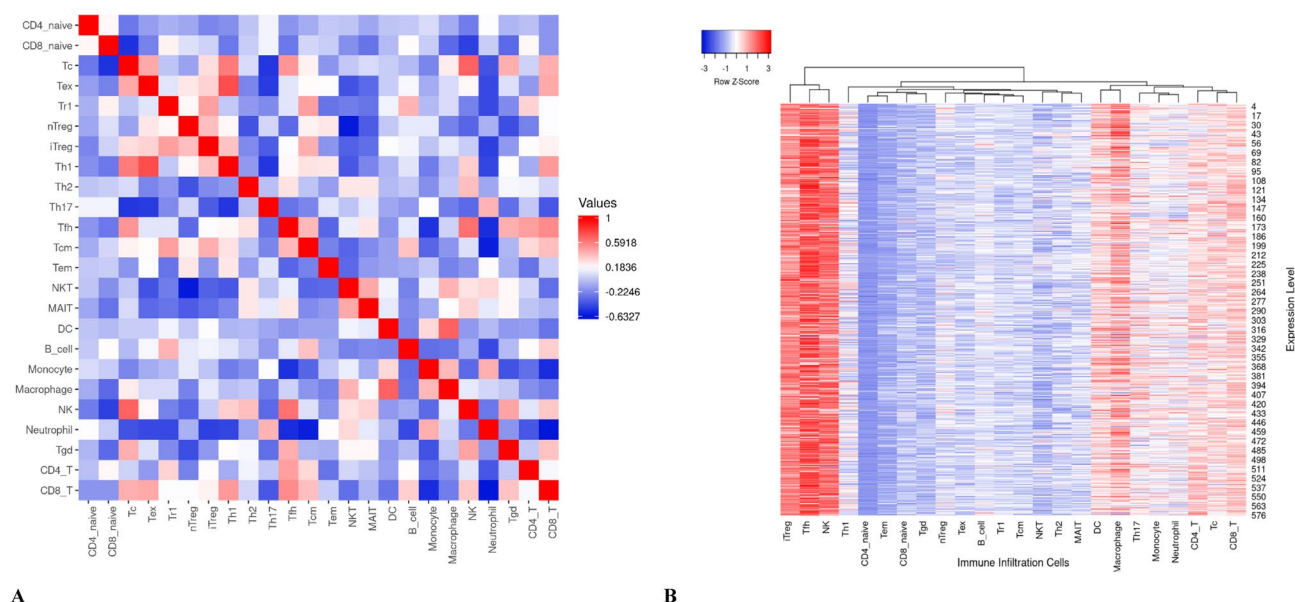


Fig. 5. Different immune infiltrating cell expression levels in LUAD samples retrieved from ImmuneCellAI. (A) Pairwise correlation values matrix for exploring the immune infiltration cells abundance in 576 samples, and (B) Heatmap presentation of the immune infiltrating cell expression levels in LUAC.

Prediction of Pioglitazone-PPARG, Telmisartan-PPARG nuclear receptor affinity and ligand efficiency

The Zinc20 database^{70,71} provided numerical values for how well pioglitazone ($pKi=7.06$) and telmisartan ($pKi=5.82$) bind to their targets, supporting earlier findings that classify pioglitazone as a PPARG agonist and telmisartan as a partial agonist²³. Additionally, the ligand efficiency values from the database show the binding strengths of pioglitazone (0.41) and telmisartan (0.21).

The cheminformatics data in this study for pioglitazone and telmisartan highlights the need to create these helpful drugs in lung-derived extracellular vesicles (Lung-Exo) or inhalable exosomes for targeted delivery to lung cells, to reduce the known side effects of the repurposed drugs, and to enhance their effectiveness.

Affinity and stability studies of pioglitazone and telmisartan into the protein carrier vehicle used for lung-targeted delivery

Molecular docking and dynamics (MD) simulations are used to evaluate how well the repurposed drugs stick to their carrier vehicles and to check if the complex remains stable as it travels from where it is given to where it works.

Molecular docking studies of pioglitazone and telmisartan into the carrier vehicle used for lung-targeted delivery

Albumin has been selected as a universal carrier for hydrophobic pharmaceuticals. The diverse human cargos act as vesicles that associate with the canonical non-muscle Myosin V (MyoV) carrier, specifically its paralog VC (MyoVC) or Myo5C, which is involved in cell membrane trafficking and the intracellular transport of cargos, including exosomes, according to KEGG.

To evaluate the binding affinity scores of pioglitazone and telmisartan to human serum albumin and extracellular exosome carrier protein for targeted pulmonary drug delivery, the albumin protein carrier was sourced from the RCSB Protein Data Bank (RCSB PDB) under PDB code 1HK1, which represents human serum albumin (HSA) complexed with thyroxine (3,3',5,5'-tetraiodo-L-thyronine)⁷². The cargo binding domain from human MyoVC was obtained from the Peptide Atlas⁷³ with PDB code 4L8T, which does not contain a crystallized ligand⁷⁴.

We identified the optimal location within the cargo-binding domain of the transporter protein to accommodate the tested pharmaceuticals, enabling an assessment of their compatibility following docking simulations. We selected the pocket with the highest amino acid content and largest dimensions to ensure compatibility with the shape of the target medicines for docking. The pocket selected exhibited the highest amino acid count and largest dimensions, thereby ensuring compatibility with the contoured surface of the target medicines for docking. Conversely, we incorporated these two medications directly into the albumin carrier to facilitate the targeted delivery of thyroxine (T4) within the body.

The docking results demonstrated that both pioglitazone and telmisartan exhibit strong binding to MyoVc and albumin carriers (Fig. 8), indicating that their interactions with the amino acids at the binding sites of these proteins contribute to the observed high-affinity scores. The findings demonstrate that both drugs effectively treat lung cancer, necessitating reduced doses and less frequent administration. Additionally, the human MyoVc cargo-binding domain transporter can deliver telmisartan to lung tissues for cancer therapy. Our findings indicate that pioglitazone exhibits weaker binding and attraction at the albumin site, suggesting it is less stable compared to telmisartan.

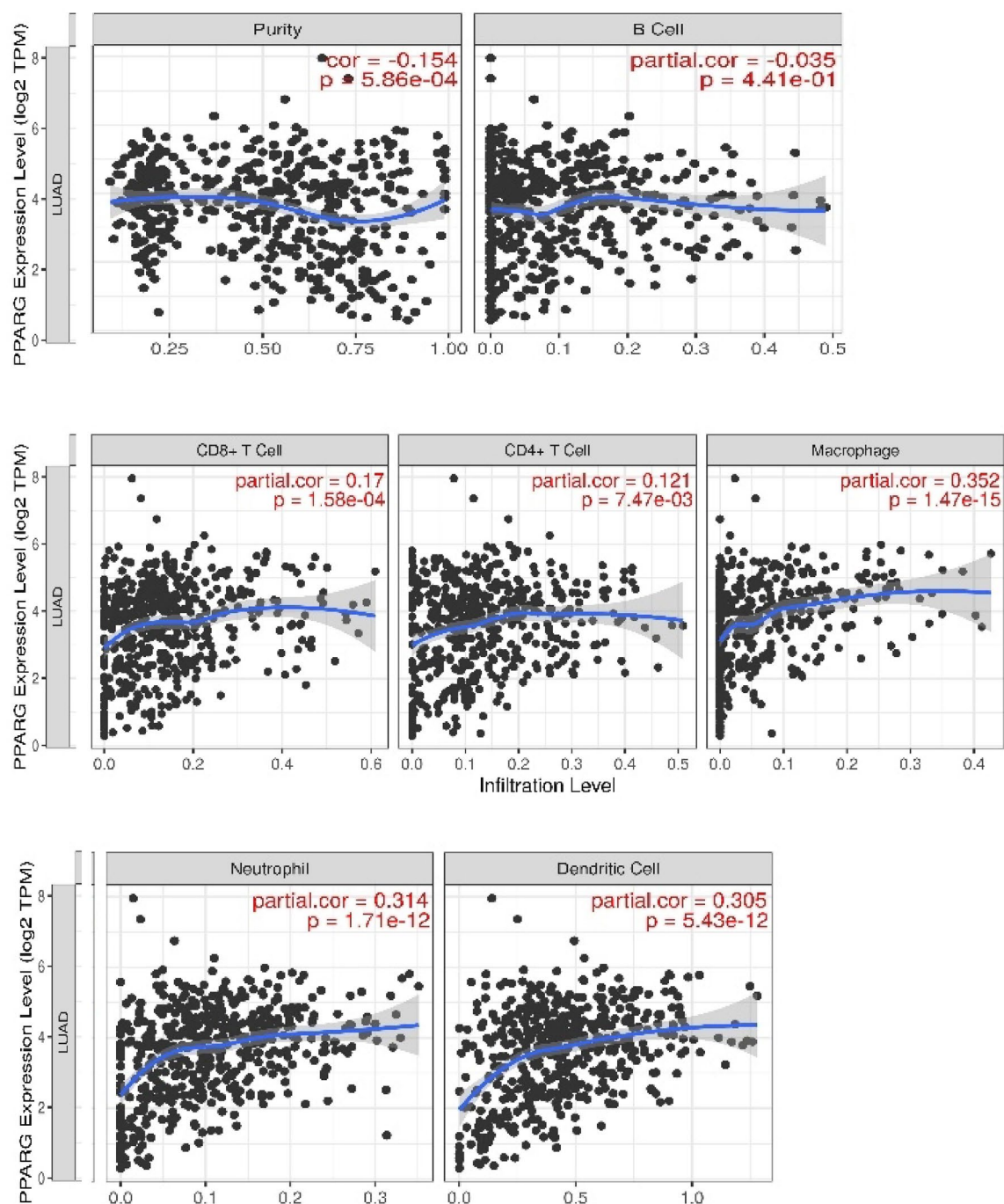


Fig. 6. Correlation values of PPARG gene expression level (expressed as log2 TPM) with the tumor immune infiltration cells level in LUAD.

Figure 9 presents 2D-style docking solutions for pioglitazone, telmisartan, and T4 within the cargo domain of MyoVc (PDB entry 4L8T) vesicles (exosomes) in the upper panel and albumin (PDB entry 1HK1) in the middle panel, alongside albumin complexed with T4 (the original ligand) in the lower panel. The three-letter and digit protein sequence code denotes amino acid residues, whereas the green and blue dotted lines classify contact forces following the figure's descriptive scheme.

MD simulation of telmisartan in complex with cargo binding domain from human MyoVc

We ran molecular dynamics simulations of the telmisartan-human MyoVc cargo-binding domain complex to study how the protein behaves and changes at the atomic level for 18 nanoseconds. The intricate system reached equilibrium within 1 ns, demonstrating stable atomic fluctuations within 17 ns of the simulation's duration. This verifies that the simulation time was adequate for the aims of the present investigation, designated as a “TDDS study⁷⁵”.

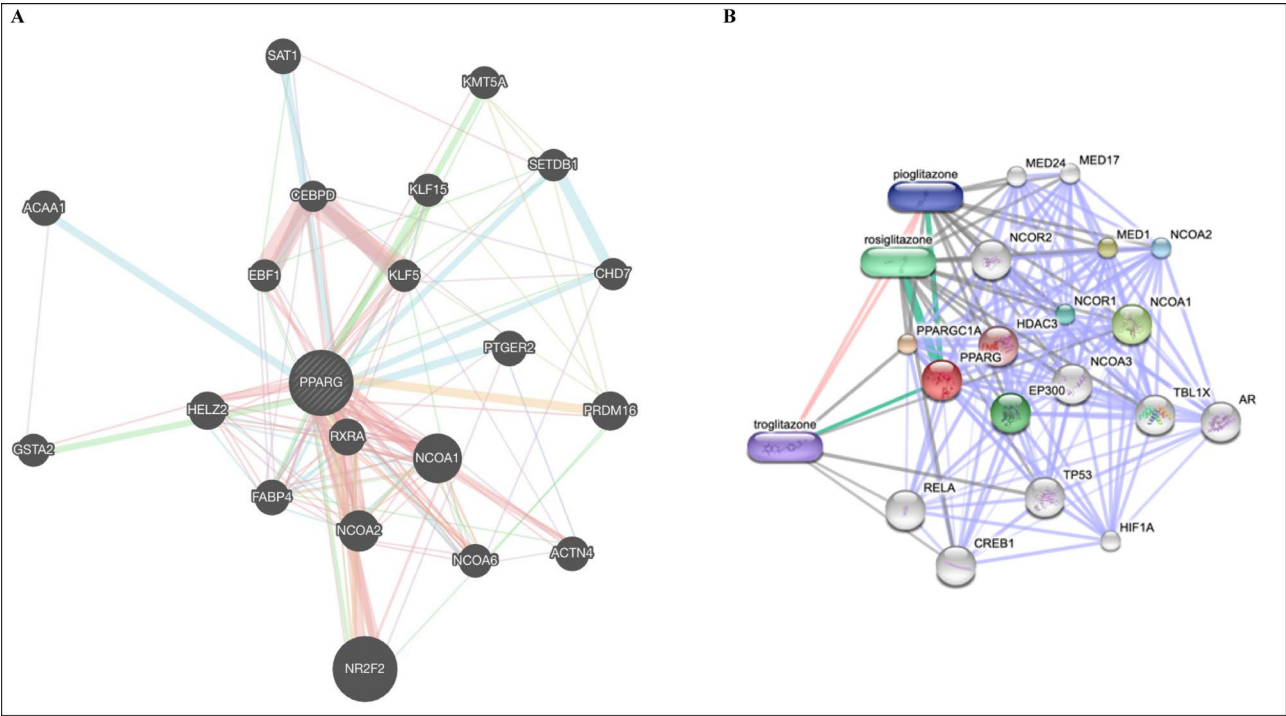


Fig. 7. (A) The GeneMANIA presentation of PPARG’s protein-protein interaction (PPI) network shows networks for physical interactions between genes as pink lines, co-expression as violet lines, predictions as yellow lines, common route pathways as light blue lines, and genetic interactions as green lines. Additionally, shared protein domains were considered when examining these protein relationships. (B) The STITCH presentation of PPARG predicted functional partners’ networks.

Parameter	Pioglitazone	Telmisartan	Comment
LogP (W/O)	3.021	6.249	Optimum
TPSA (Å²)	68.290	72.940	Lipophilic
PPB	97.171%	98.951%	Strong binder
Respiratory Toxicity	--	--	Non-toxic
SR-MMP	++	++	Active
NR-Aromatase	+++	++	Active
NR-AhR	+	+	Active
H-HT	++	+++	Hepatotoxic
DILI	+++	+++	Hepatotoxic

Table 2. The predicted physicochemical property and TOX21 of Pioglitazone and Telmisartan. [LogP: partition coefficient, o/w: octanol/water, TPSA: topological polar surface area, PPB: Plasma Protein Binding, SR-MMP: Mitochondrial Membrane Potential, NR-AhR: nuclear receptor-aryl hydrocarbon receptor, H-HT: human hepatotoxicity, DILI: drug-induced liver injury].

Solvation and Equilibration of the Complex

Figure 9 presents a comprehensive structural analysis of the protein-ligand complex, showcasing the solvated human MyoVc cargo binding domain in conjunction with the Telmisartan complex, along with the equilibrated states of the protein-ligand complex collected at different phases of the simulation. The subsequent perspective of the complex illustrates various approaches to examining the simulated conditions of the protein-ligand complex (MyoVc-telmisartan).

Root-Mean Square Deviations (RMSD)

An essential component of our research entailed examining the stability and conformational alterations of the complex, protein, and ligand separately. Figure 10 displays the RMSD values for the complex, protein, and ligand, respectively. These graphs illustrate three separate stages in the execution of molecular dynamics simulations.

The initial phase, lasting 2 ns, includes 50,000 steps of energy minimization. A 0.5 ns duration of incremental heating elevates the system to ambient temperature. We then utilized a 1 ns equilibration phase to steady the

Drug	Target	Common Name	CHEMBL ID
Pioglitazone	PPARG	Peroxisome proliferator-activated receptor gamma	CHEMBL235
	MAOB	Monoamine oxidase B	CHEMBL2039
	CA2	Carbonic anhydrase II	CHEMBL205
	AGTR1	Type-1 angiotensin II receptor	CHEMBL227
	PPARA	Peroxisome proliferator-activated receptor alpha	CHEMBL239
	ABCB11	Bile salt export pump	CHEMBL6020
Telmisartan	ACE	Angiotensin-converting enzyme	CHEMBL1808
	AGTR1	Type-1 angiotensin II receptor	CHEMBL227
	PPARG	Peroxisome proliferator-activated receptor gamma	CHEMBL235
	AGTR2	Angiotensin II receptor	CHEMBL4607
	GLRA1	Glycine receptor subunit alpha 1	CHEMBL5845

Table 3. Predicted Pioglitazone and Telmisartan biological targets of the highest probability.

Drug	Gene Name	Class	pKi (L.E.)
Pioglitazone	PPARG (agonist)	Transcription factor/NR	7.06 (0.40)
Telmisartan			5.82 (0.21)

Table 4. Predicted Pioglitazone and Telmisartan binding affinity and ligand efficiency.

system. The concluding step of our simulation method was a prolonged (17 ns) duration of production molecular dynamics simulations, during which the most notable dynamic characteristics of the complex were observed and assessed.

The RMSD analysis of MD simulations for the protein transporter complex (Fig. 10A), apoprotein (Fig. 10B), and ligand (Fig. 10C) showed that telmisartan can likely stay attached to the human MyoVc cargo-binding domain at the specific pocket shown in Fig. 8.

Beta Factor Analysis of Protein Backbone Atoms

To demonstrate the flexibility of the protein backbone atoms and the interactions of telmisartan with the human MyoVc cargo-binding domain within the binding site⁷⁶, we assessed the beta factor of the protein complex throughout molecular dynamics simulations concerning the positions of the protein residues⁷⁷. The highest beta factor values, illustrated in the beta factor plot (Fig. 11), were observed at residue numbers 155–180 (auth: 1450–1475), indicating concordance with the contact force established with His 155 (auth: His 1450), as represented by the extracted docking solution of Telmisartan (Fig. 8). Additionally, various protein residue numbers exhibited significant changes in atomic motion during the simulation compared to the initial atomic trajectories at 30–40 (auth: 1325–1335), 105–115 (auth: 1400–1410), and 300–345 (auth: 1595–1640). The graphical representation of the beta factor for the protein complex (Fig. 11) confirmed the flexibility of the protein transporter’s active site in the presence of telmisartan and its atomic interactions. Previous research has investigated the anti-lung cancer effects of TZDs in clinical settings; however, the most effective PPARG agonist, rosiglitazone, exhibits specific undesirable effects, unlike pioglitazone. The side effects of the partial PPARG agonist, telmisartan, are infrequent; however, its gene expression profiles confer superior anti-tumor benefits. In the present study, telmisartan was recognized as an appropriate candidate for the “Beta Factor Analysis” of the human MyoVc cargo binding domain protein during molecular dynamics simulations, which elucidated the stability and flexibility of the MyoVc protein-drug complex and its interaction dynamics with telmisartan.

Conclusion

The activation of the PPARG transcription factor is linked to reduced NSCLC growth. Research indicates that pioglitazone and telmisartan are potential therapies for NSCLC due to their PPARG-agonistic properties. There is a critical need for new targeted drug delivery formulations for these drugs to minimize systemic toxicity. The study suggests using extracellular vesicles from lung tissue for targeted drug delivery to pulmonary cancer cells. Bioinformatics and cheminformatics data support pioglitazone and telmisartan as promising repurposed drugs for LUAC, highlighting their lipophilicity and compatibility with exosomal components like albumin. Cheminformatics also pointed out potential off-target effects and hepatotoxicity, emphasizing the importance of exosomal targeted delivery. Molecular docking and MD simulations confirmed the affinity and stability of drug-exosomal vehicle complexes. The proposed engineering of exosomal cargo for targeted delivery of these drugs to lung cells could enhance NSCLC treatment and address drug resistance while minimizing systemic toxicity. Finally, the study’s computational technique saves the researchers time and money when building formulations containing biological components for targeted drug delivery.

Nonetheless, experimental validation is on the way as the sustainability of the current manuscript, to emphasize the success of the suggested formulation based on computational work (a limitation).

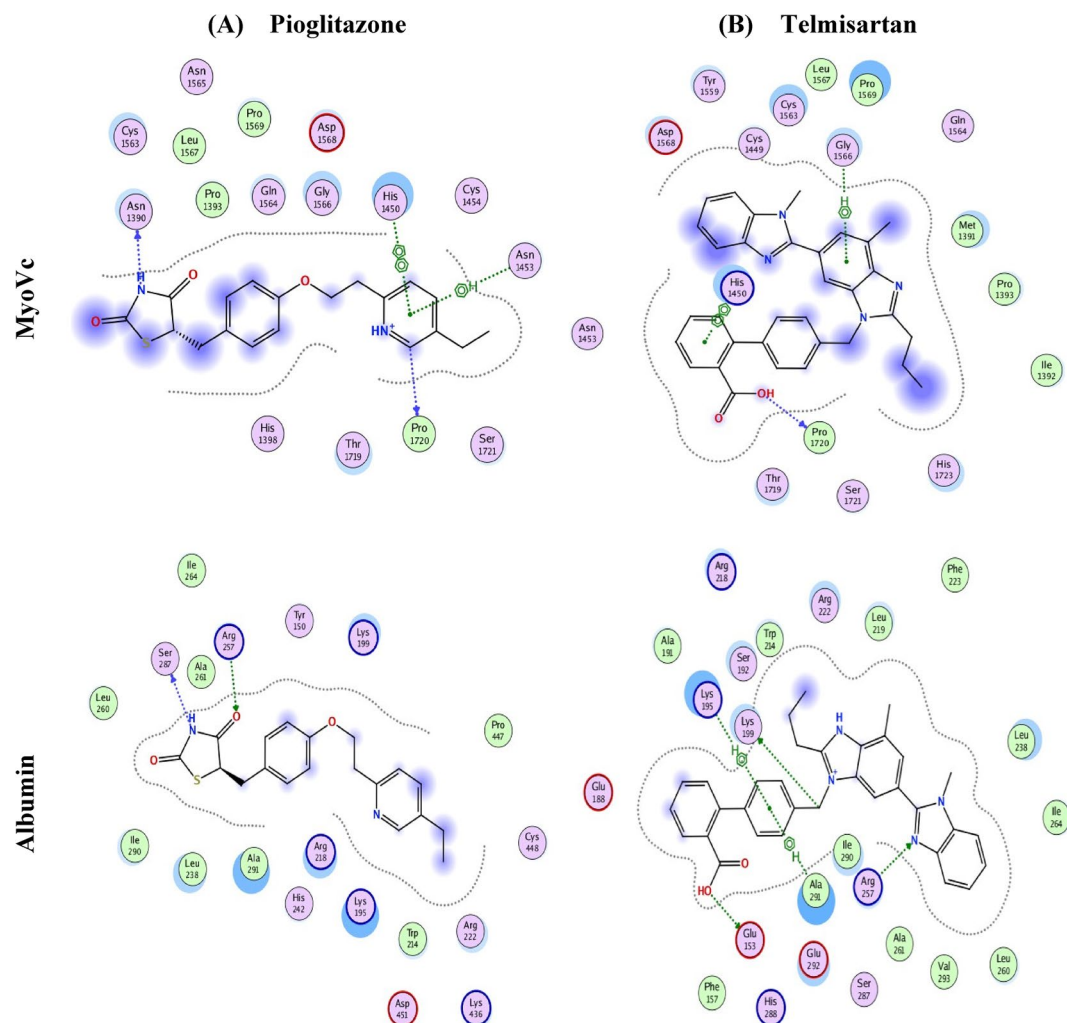


Fig. 8. Affinity in complex with Cargo domain of MyoVc (pdb entry 4L8T) vesicles (exosomes) (upper panel) and in complex with albumin (pdb entry 1HK1) (middle panel) compared to albumin carrying T4 (the original ligand) (lower figure). Blue and green dotted arrows and green dots present hydrophobic interactions and hydrogen bonding forces.

Recommendation. Repurposing PPARG-agonist drugs with or without co-supplementary vitamins with tumor-modulatory effects and positive impact on various disease metabolic/inflammatory pathways as vitamin D⁷⁸ would be crucial point to study as well.

T4

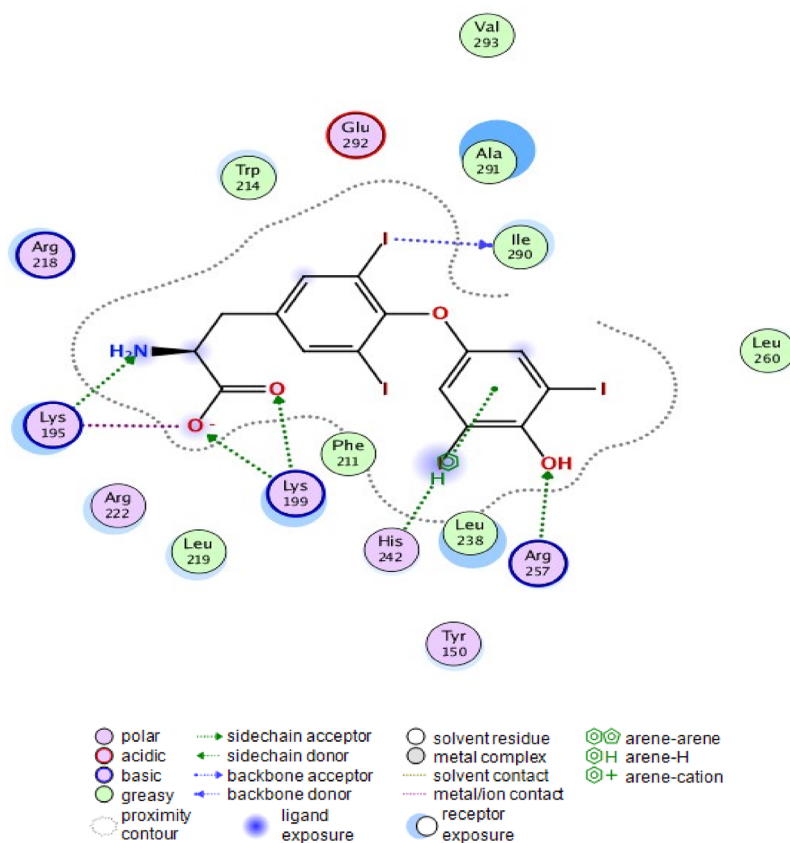


Fig. 8. (continued)

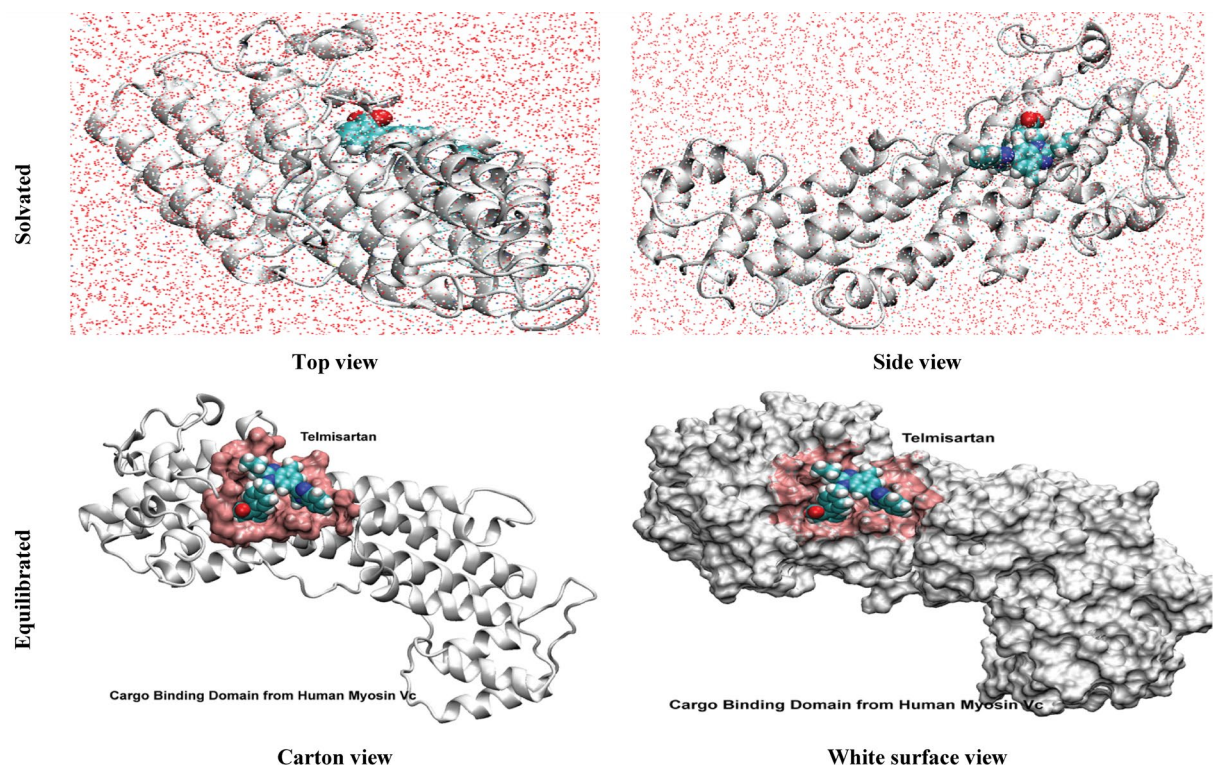


Fig. 9. Human MyoVc Cargo Binding Domain and Telmisartan Solvated (upper panel) complex top and side views and equilibrated complex (lower panel) shown in a carton view or with a white surface view with Telmisartan in blue within the pink binding pocket.

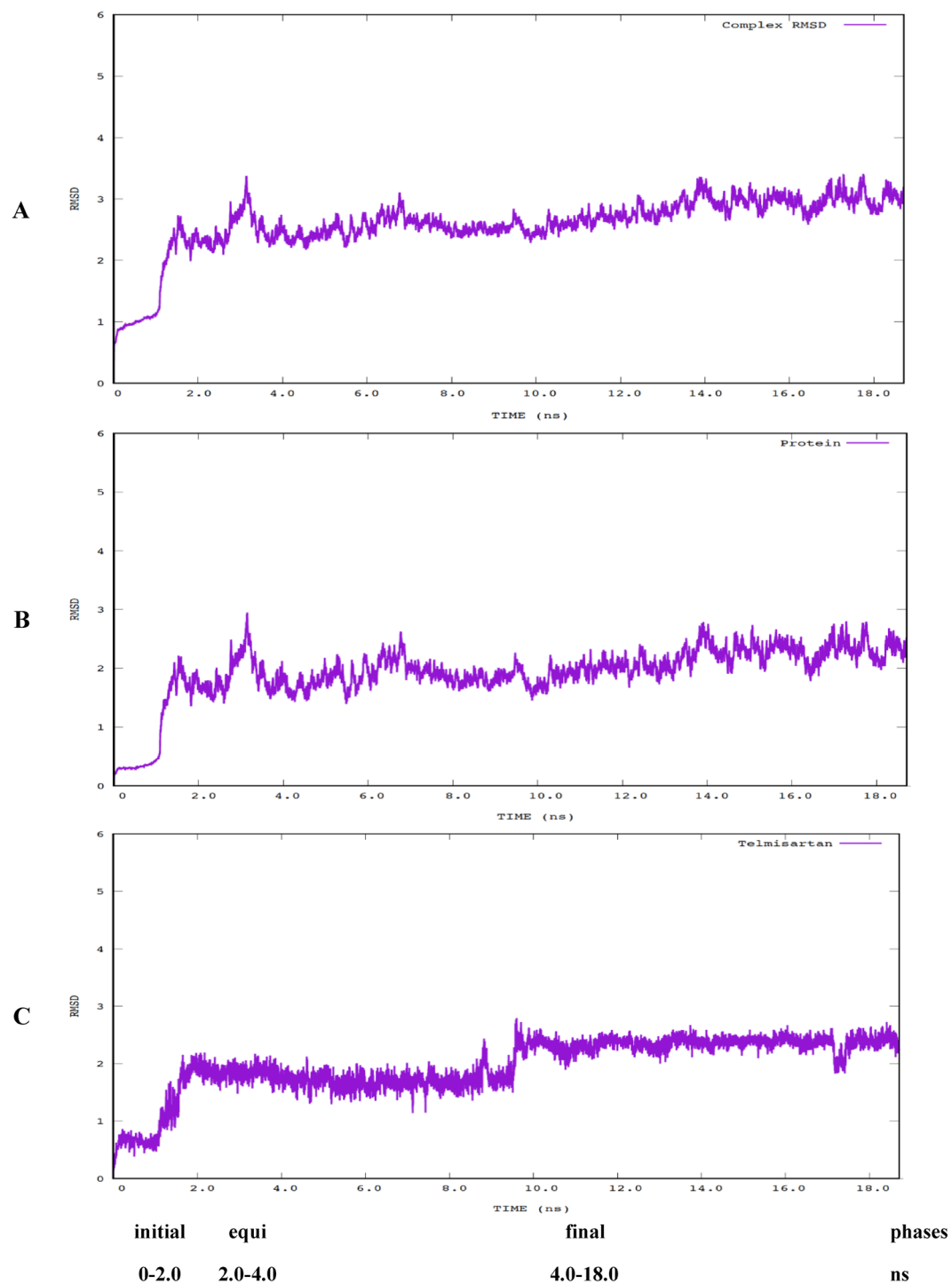


Fig. 10. The RMSD graph for the human (A) MyoVc Cargo Binding Domain and Telmisartan complex, (B) MyoVc Cargo Binding Domain protein only, and (C) Telmisartan.

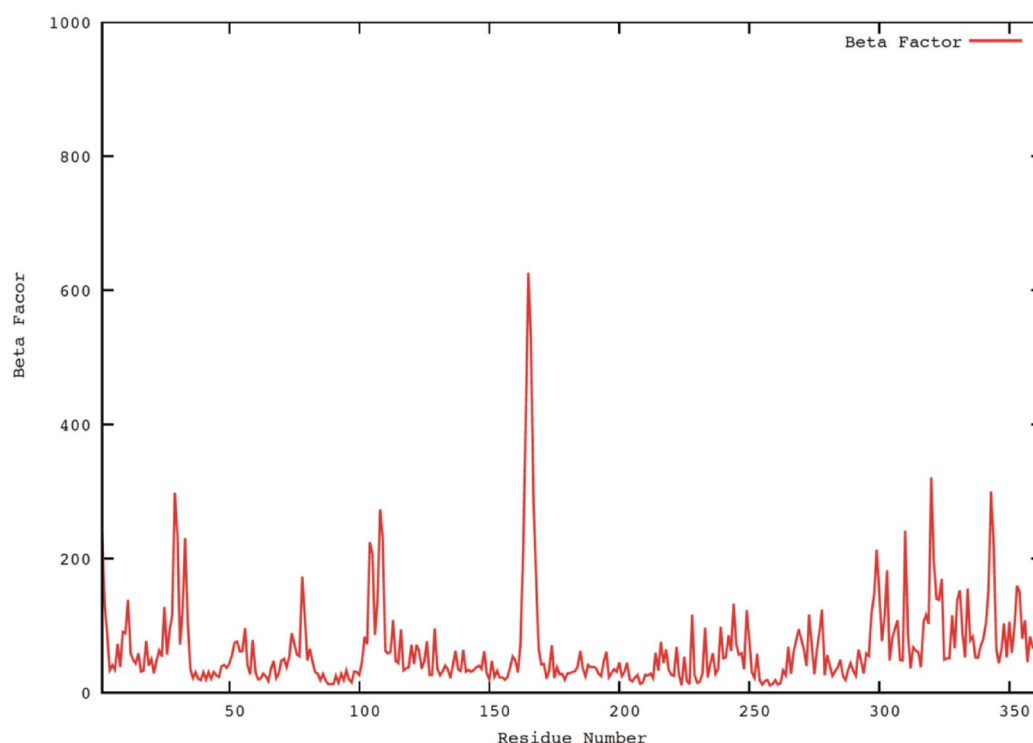


Fig. 11. The average atomic fluctuations (Beta Factor) of the Human MyoVc Cargo Binding Domain protein during the molecular dynamic simulations.

Data availability

“No data is generated, all data are incorporated within the manuscript, for any queries the corresponding authors to be contacted”.

Received: 11 February 2025; Accepted: 3 July 2025

Published online: 11 July 2025

References

- Hamdy, N. M., Eskander, G. & Basalious, E. B. Insights on the dynamic innovative tumor Targeted-Nanoparticles-Based drug delivery systems activation techniques. *Int. J. Nanomed.*, 17, 6131–6155 (2022).
- Hamdy, N. M., Boseila, A. A., Ramadan, A. & Basalious, E. B. Iron Oxide Nanoparticles-Plant Insignia Synthesis with Favorable Biomedical Activities and Less Toxicity, in the Era of the-Green: A Systematic Review. LID – 10.3390/pharmaceutics14040844 [doi] LID – 844, *Pharmaceutics*, 14 844. (2022).
- Rostamabadi, H., Falsafi, S. R. & Jafari, S. M. Nanoencapsulation of carotenoids within lipid-based nanocarriers. *J. Controlled Release: Official J. Controlled Release Soc.* **298**, 38–67 (2019).
- Sánchez-López, E., Gómar, M. J. & Haro, I. Nanotechnology-Based platforms for vaginal delivery of peptide microbicides. *Curr. Med. Chem.* **28**, 4356–4379 (2021).
- Herrmann, I. K., Wood, M. J. A. & Fuhrmann, G. Extracellular vesicles as a next-generation drug delivery platform. *Nat. Nanotechnol.* **16**, 748–759 (2021).
- Chen, G. et al. LncRNADisease: a database for long-non-coding RNA-associated diseases. *Nucleic Acids Res.* **41**, D983–986 (2013).
- Kanehisa, M., Sato, Y., Kawashima, M., Furumichi, M. & Tanabe, M. KEGG as a reference resource for gene and protein annotation. *Nucleic Acids Res.* **44**, D457–462 (2016).
- Tsubouchi, Y. et al. Inhibition of human lung cancer cell growth by the peroxisome proliferator-activated receptor-gamma agonists through induction of apoptosis. *Biochemical and Biophysical Research Communications* **270** 400–405. (2000).
- Chang, T. H. & Szabo, E. Induction of differentiation and apoptosis by ligands of peroxisome proliferator-activated receptor gamma in non-small cell lung cancer. *Cancer Res.* **60**, 1129–1138 (2000).
- Wick, M. et al. Peroxisome proliferator-activated receptor-gamma is a target of nonsteroidal anti-inflammatory drugs mediating cyclooxygenase-independent Inhibition of lung cancer cell growth. *Mol. Cell. Biol.* **24**, 8691–8704 (2004).
- Keshamouni, V. G. et al. Peroxisome proliferator-activated receptor-gamma activation inhibits tumor progression in non-small-cell lung cancer. *Oncogene* **23**, 100–108 (2004).
- Keshamouni, V. G. et al. PPAR-gamma activation inhibits angiogenesis by blocking ELR + CXC chemokine production in non-small cell lung cancer. *Neoplasia (New York N Y)*. **7**, 294–301 (2005).
- Akaike, M. et al. The hinge-helix 1 region of peroxisome proliferator-activated receptor gamma1 (PPARgamma1) mediates interaction with extracellular signal-regulated kinase 5 and PPARgamma1 transcriptional activation: involvement in flow-induced PPARgamma activation in endothelial cells. *Mol. Cell. Biol.* **24**, 8691–8704 (2004).
- Winn, R. A. et al. Antitumorigenic effect of Wnt 7a and Fzd 9 in non-small cell lung cancer cells is mediated through ERK-5-dependent activation of peroxisome proliferator-activated receptor gamma. *J. Biol. Chem.* **281**, 26943–26950 (2006).
- Öztürk, N. A. O., Kara, A. A. O. & Vural, A. O. İ. Formulation and In Vitro Evaluation of Telmisartan Nanoparticles Prepared by Emulsion-Solvent Evaporation Technique, (2020).

16. Mostafa, A. M., Hamdy, N. M., Abdel-Rahman, S. Z. & El-Mesallamy, H. O. Effect of vildagliptin and Pravastatin combination on cholesterol efflux in adipocytes. *IUBMB Life*. **68**, 535–543 (2016).
17. Mostafa, A. M., Hamdy, N. M., El-Mesallamy, H. O. & Abdel-Rahman, S. Z. Glucagon-like peptide 1 (GLP-1)-based therapy upregulates LXR-ABCA1/ABCG1 cascade in adipocytes. *Biochem. Biophys. Res. Commun.* **468**, 900–905 (2015).
18. Anis, A., Mostafa, A., Kerema, M. S., Hamdy, N. M. & Sultan, A. S. In Silico and cheminformatics prediction with experimental validation of an adipogenesis cocktail, Sorafenib with Rosiglitazone for HCC dedifferentiation. *J. Genetic Eng. Biotechnol.* **22** (4), 100429 (2024).
19. Sasaki, H. et al. Decreased peroxisome proliferator-activated receptor gamma gene expression was correlated with poor prognosis in patients with lung cancer. *Lung cancer (Amsterdam Netherlands)*. **36**, 71–76 (2002).
20. Ciaramella, V. et al. Activity and molecular targets of Pioglitazone via Blockade of proliferation, invasiveness and bioenergetics in human NSCLC. *J. Exp. Clin. Cancer Res.* **38**, 178 (2019).
21. Stark, C., Breitkreutz, B. J., Reguly, T., Boucher, L. & Breitkreutz, A. Tyers, biogrid: a general repository for interaction datasets. *Nucleic Acids Res.* **34**, D535–539 (2006).
22. Ru, B. et al. TISIDB: an integrated repository portal for tumor-immune system interactions. *Bioinformatics* **35**, 4200–4202 (2019).
23. Ayza, M. A., Zewdie, K. A., Tesfaye, B. A., Gebrekirstos, S. T. & Berhe, D. F. Anti-Diabetic effect of Telmisartan through its partial PPAR γ -Agonistic activity. *Diabetes Metabolic Syndrome Obesity: Targets Therapy*. **13**, 3627–3635 (2020).
24. Amano, Y. et al. Structural basis for telmisartan-mediated partial activation of PPAR gamma. *Hypertens. Research: Official J. Japanese Soc. Hypertens.* **35**, 715–719 (2012).
25. Maejima, Y. et al. Telmisartan, a unique ARB, improves left ventricular remodeling of infarcted heart by activating PPAR gamma. *Lab. Invest.* **91**, 932–944 (2011).
26. Rasheduzzaman, M., Moon, J. H., Lee, J. H., Nazim, U. M. & Park, S. Y. Telmisartan generates ROS-dependent upregulation of death receptor 5 to sensitize TRAIL in lung cancer via Inhibition of autophagy flux. *Int. J. Biochem. Cell Biol.* **102**, 20–30 (2018).
27. Surapaneni, S. K. et al. Telmisartan facilitates the anticancer effects of CARP-1 functional mimetic and Sorafenib in roscitinin resistant Non-small cell lung Cancer. *Anticancer Res.* **41**, 4215–4228 (2021).
28. Zhang, S. & Wang, Y. Telmisartan inhibits NSCLC A549 cell proliferation and migration by regulating the PI3K/AKT signaling pathway. *Oncol. Lett.* **15**, 5859–5864 (2018).
29. Jafari, D. et al. Designer exosomes: A new platform for biotechnology therapeutics. *BioDrugs* **34**, 567–586 (2020).
30. Wang, Z., Wang, Q., Qin, F. & Chen, J. Exosomes: a promising avenue for cancer diagnosis beyond treatment. *Front. Cell. Dev. Biology*. **12**, 1344705 (2024).
31. Kar, R. et al. Exosome-Based smart drug delivery tool for Cancer theranostics. *ACS Biomaterials Sci. Eng.* **9**, 577–594 (2023).
32. Zhang, M. et al. Engineered exosomes from different sources for cancer-targeted therapy. *Signal. Transduct. Target. Therapy*. **8**, 124 (2023).
33. Keerthikumar, S. et al. ExoCarta: A Web-Based compendium of Exosomal cargo. *J. Mol. Biol.* **428**, 688–692 (2016).
34. Lv, Y. et al. Nonmuscle myosin heavy chain IIA-Mediated exosome release via regulation of the Rho-Associated kinase 1/myosin light chains/Actin pathway. *Front. Pharmacol.* **11**, 598592 (2020).
35. Bhattacharya, K. et al. Multi-Epitope Vaccine Design against Monkeypox Virus via Reverse Vaccinology Method Exploiting Immunoinformatic and Bioinformatic Approaches, 10 2010. (2022).
36. Karlsson M, Zhang C, Méar L, et al. A single-cell type transcriptomics map of human tissues. *Sci Adv.* **7** (31), eabh2169 (2021). <https://doi.org/10.1126/sciadv.abh2169>
37. Chandrashekar, D. S. et al. UALCAN: an update to the integrated cancer data analysis platform. *Neoplasia (New York N Y)*. **25**, 18–27 (2022).
38. Sobin, L. et al. Histologic and Quality Assessment of Genotype-Tissue Expression (GTEx) Research Samples: A Large Postmortem Tissue Collection, Archives of pathology & laboratory medicine, (2024).
39. Rockweiler N.B. et al. The origins and functional effects of postzygotic mutations throughout the human life span. *Sci. (New York N Y)*. **380**, eabn7113 (2023).
40. Tang, Z. et al. GEPIA: a web server for cancer and normal gene expression profiling and interactive analyses. *Nucleic Acids Res.* **45**, W98–W102 (2017).
41. Miao, Y. R. et al. ImmCellAI: A unique method for comprehensive T-Cell subsets abundance prediction and its application in Cancer immunotherapy. *Adv. Sci. (Weinh)*. **7**, 1902880 (2020).
42. Li, T. et al. TIMER: A web server for comprehensive analysis of Tumor-Infiltrating immune cells. *Cancer Res.* **77**, e108–e110 (2017).
43. Warde-Farley, D. et al. The genemania prediction server: biological network integration for gene prioritization and predicting gene function. *Nucleic Acids Res.* **38**, W214–W220 (2010).
44. Kouranov, A. et al. The RCSB PDB information portal for structural genomics. *Nucleic Acids Res.* **34**, D302–D305 (2006).
45. Innis, C. A. siteFINDER|3D: a web-based tool for predicting the location of functional sites in proteins. *Nucleic Acids Res.* **35**, W489–W494 (2007).
46. Ragab, M. A. et al. Structure-based design and synthesis of conformationally constrained derivatives of methyl-piperidinopyrazole (MPP) with Estrogen receptor (ER) antagonist activity. *Bioorg. Chem.* **119**, 105554 (2022).
47. Cramer, C. J. (2006).
48. Wang, J., Wolf, R. M., Caldwell, J. W., Kollman, P. A. & Case, D. A. Development and testing of a general AMBER force field. *J. Comput. Chem.* **25**, 1157–1174 (2004).
49. Anwar, M. M., Albanese, C., Hamdy, N. M. & Sultan, A. S. Rise of the natural red pigment ‘prodigiosin’ as an Immunomodulator in cancer. *Cancer Cell Int.* **22**, 419 (2022).
50. Khodair, A. I. et al. Camptothecin structure simplification elaborated new imidazo[2,1-b]quinazoline derivative as a human topoisomerase I inhibitor with efficacy against bone cancer cells and colon adenocarcinoma. *Eur. J. Med. Chem.* **265**, 116049 (2024).
51. Chiang, Y. F. et al. Hinokitiol inhibits breast Cancer cells in vitro Stemness-Progression and Self-Renewal with apoptosis and autophagy modulation via the CD44/Nanog/SOX2/Oct4 pathway. *Int. J. Mol. Sci.*, **25**(7), 3904 (2024).
52. Atta, H. et al. New trends in synthetic drugs and natural products targeting 20S proteasomes in cancers. *Bioorg. Chem.* **133**, 106427 (2023).
53. El Mesallamy, H. O., Rashed, W. M., Hamdy, N. M. & Hamdy, N. High-dose methotrexate in Egyptian pediatric acute lymphoblastic leukemia: the impact of ABCG2 C421A genetic polymorphism on plasma levels, what is next? *J. Cancer Res. Clin. Oncol.* **140**, 1359–1365 (2014).
54. Zhang, J., Tang, M. & Shang, J. PPAR γ modulators in lung cancer: molecular mechanisms, clinical prospects, and challenges. *Biomolecules* **14** 190. (2024).
55. Daniil, S. et al. Differential signaling pathways in medulloblastoma: Nano-biomedicine targeting Non-coding epigenetics to improve current and future therapeutics. *Curr. Pharm. Design.* **30**, 31–47 (2024).
56. Rizk, N. I. et al. Revealing the role of serum Exosomal novel long non-coding RNA NAMPT-AS as a promising diagnostic/prognostic biomarker in colorectal cancer patients. *Life Sci.* **352**, 122850 (2024).
57. Azimi, F. et al. Tumor-infiltrating lymphocyte grade is an independent predictor of Sentinel lymph node status and survival in patients with cutaneous melanoma. *J. Clin. Oncol.* **30**, 2678–2683 (2012).
58. Kaur, S., Nag, A., Gangenahalli, G. & Sharma, K. Peroxisome proliferator activated receptor gamma sensitizes Non-small cell lung carcinoma to gamma irradiation induced apoptosis. *Front. Genet.*, **10**, 554 (2019).

59. Hirohara, M., Saito, Y., Koda, Y., Sato, K. & Sakakibara, Y. Convolutional neural network based on SMILES representation of compounds for detecting chemical motif. *BMC Bioinform.* **19**, 526 (2018).
60. Xiong, G. et al. ADMETLab 2.0: an integrated online platform for accurate and comprehensive predictions of ADMET properties. *Nucleic Acids Res.* **49**, W5–W14 (2021).
61. Jiang, D. et al. ADMET evaluation in drug discovery. 20. Prediction of breast cancer resistance protein Inhibition through machine learning. *J. Cheminform.* **12**, 16 (2020).
62. Kharkar, P. S. Drugs acting on central nervous system (CNS) targets as leads for non-CNS targets. *F1000Research* **3**, 40 (2014).
63. Hitchcock, S. A. & Pennington, L. D. Structure-brain exposure relationships. *J. Med. Chem.* **49**, 7559–7583 (2006).
64. Julie, N. L., Julie, I. M., Kende, A. I. & Wilson, G. L. Mitochondrial dysfunction and delayed hepatotoxicity: another lesson from troglitazone. *Diabetologia* **51**, 2108–2116 (2008).
65. Floyd, J. S., Barbehenn, E., Lurie, P. & Wolfe, S. M. Case series of liver failure associated with Rosiglitazone and Pioglitazone. *Pharmacoepidemiol. Drug Saf.* **18**, 1238–1243 (2009).
66. May, L. D., Lefkowitz, J. H., Kram, M. T. & Rubin, D. E. Mixed hepatocellular-cholestatic liver injury after Pioglitazone therapy. *Ann. Intern. Med.* **136**, 449–452 (2002).
67. Daina, A., Michielin, O. & Zoete, V. SwissTargetPrediction: updated data and new features for efficient prediction of protein targets of small molecules. *Nucleic Acids Res.* **47**, W357–W364 (2019).
68. Daina, A. & Zoete, V. Testing the predictive power of reverse screening to infer drug targets, with the help of machine learning. *Commun. Chem.* **7**, 105 (2024).
69. Šilhavý, J. et al. Acute toxic effects of Telmisartan in spontaneously hypertensive rats fed a high Fructose diet. *Physiol. Res.* **67**, 851–856 (2018).
70. Irwin, J. J. et al. ZINC20—A free Ultralarge-Scale chemical database for ligand discovery. *J. Chem. Inf. Model.* **60**, 6065–6073 (2020).
71. Irwin, J. J. & Shoichet, B. K. ZINC—a free database of commercially available compounds for virtual screening. *J. Chem. Inf. Model.* **45**, 177–182 (2005).
72. Petitpas, I. et al. Structural basis of albumin-thyroxine interactions and Familial dysalbuminemic hyperthyroxinemia. *Proc. Natl. Acad. Sci. U.S.A.* **100**, 6440–6445 (2003).
73. Desiere, F. et al. The PeptideAtlas project. *Nucleic Acids Res.* **34**, D655–D658 (2006).
74. Nascimento, A. F. Z. et al. Structural insights into functional overlapping and differentiation among myosin V motors. *J. Biol. Chem.* **288**, 34131–34145 (2013).
75. Hernández-Rodríguez, M., Correa-Basurto, J., Gutiérrez, A., Vitorica, J. & Rosales-Hernández, M. C. Asp32 and Asp228 determine the selective Inhibition of BACE1 as shown by Docking and molecular dynamics simulations. *Eur. J. Med. Chem.* **124**, 1142–1154 (2016).
76. Fang, Y. et al. Synthesis, biological evaluation, and molecular dynamics (MD) simulation studies of three novel F-18 labeled and focal adhesion kinase (FAK) targeted 5-bromo pyrimidines as radiotracers for tumor. *Eur. J. Med. Chem.* **127**, 493–508 (2017).
77. Ivanov, A. A. et al. Molecular modeling and molecular dynamics simulation of the human A2B adenosine receptor. The study of the possible binding modes of the A2B receptor antagonists. *J. Med. Chem.* **48**, 6813–6820 (2005).
78. Chen, Y. C. et al. Effect of vitamin D supplementation on primary dysmenorrhea: A systematic review and Meta-Analysis of randomized clinical trials. *Nutrients* **15** 2830. (2023).

Acknowledgements

PROTAC Scientific, Drug Discovery Pro LLC as well as the Molecular Operating Environment (MOE) software (Chemical Computing Group Inc., Quebec, Montreal, Canada).

Author contributions

Conceptualization; Hamdy NM, Kassab SE, Sanad EF, Basalious EB, Sultan AS, Writing original draft; Hamdy NM, Kassab SE, Essam M, Guirguis MA, Data curation, interpreted and discussed the results Hamdy NM, Kassab SE, Sultan AS, Hamdy NM performed in silico/Bioinformatics analysis and Cheminformatics, Kassab SE performed molecular docking, Revising and rewriting; Hamdy NM, Kassab SE, Sanad EF, Essam M, Guirguis MA, Sultan AS. All authors approved the current authorship. All authors have read and approved manuscript submissions in the current form.

Funding

Open access funding provided by The Science, Technology & Innovation Funding Authority (STDF) in cooperation with The Egyptian Knowledge Bank (EKB). STDF PGSG call 2, 2023 fund # 48782 to Guirguis MA, Sultan AS, Hamdy NM.

Declarations

Competing interests

The authors declare no competing interests.

Ethical approval

Not Applicable.

Additional information

Correspondence and requests for materials should be addressed to N.M.H. or S.E.K.

Reprints and permissions information is available at www.nature.com/reprints.

Publisher's note Springer Nature remains neutral with regard to jurisdictional claims in published maps and institutional affiliations.

Open Access This article is licensed under a Creative Commons Attribution 4.0 International License, which permits use, sharing, adaptation, distribution and reproduction in any medium or format, as long as you give appropriate credit to the original author(s) and the source, provide a link to the Creative Commons licence, and indicate if changes were made. The images or other third party material in this article are included in the article's Creative Commons licence, unless indicated otherwise in a credit line to the material. If material is not included in the article's Creative Commons licence and your intended use is not permitted by statutory regulation or exceeds the permitted use, you will need to obtain permission directly from the copyright holder. To view a copy of this licence, visit <http://creativecommons.org/licenses/by/4.0/>.

© The Author(s) 2025